Three-Electrode Device for Applying Two-Dimensional Vector Electric Fields to Single InAs Quantum Dots

Xiangyu Ma, Yuejing Wang, Joshua Zide, and Matthew Doty*
Material Science and Engineering Department, University of Delaware, Newark, Delaware 19716, USA

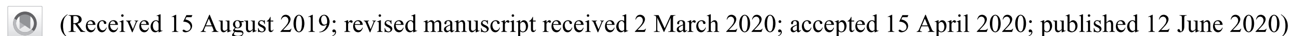
(Received 15 August 2019; revised manuscript received 2 March 2020; accepted 15 April 2020; published 12 June 2020)

Electric field tuning of single InAs quantum dots (QDs) provides an important tool for physics experiments and for the development of scalable and *in situ*–tunable devices. Control of a single QD with either a growth direction or an in-plane electric field is well established, but a device that can apply the two-dimensional (2D) vector electric fields necessary to simultaneously and independently tune more than one parameter has not yet been demonstrated. We use COMSOL MULTIPHYSICS simulations to illustrate the device-design challenges in applying a uniform 2D electric field in a GaAs solid-state system and to systematically explore the effects of electrode coverage, mesa size, and doping on the device performance. We develop and present a design that can apply 2D electric fields to a single QD while remaining compatible with optical experiments. We then fabricate and characterize a proof-of-concept device that validates the design presented here. We discuss the applications for this device and the potential for full 2D-electric-field control of a single QD or a quantum-dot molecule.

DOI: 10.1103/PhysRevApplied.13.064029

I. INTRODUCTION

InAs quantum dots (QDs) and quantum-dot molecules (QDMs) grown in GaAs heterostructures by molecular beam epitaxy (MBE) have excellent optical properties and have long been of interest for incorporation into quantum optoelectronic devices for applications such as single-photon generation [1–3], spin-photon coupling [4–6], and spin manipulation [7,8]. A scalable platform for quantum optics or quantum computing requires a large number of identical quantum emitters, spin units, and so forth. However, the random nucleation of the Stranski-Krastanov MBE growth process typically leads to QDs and QDMs with different sizes, shapes, and geometries [9–11]. External electric fields are commonly used to fine-tune the optical properties of a QD to overcome these variations and to control the charge occupancy of the QD. Specifically, a QD is usually charged with electrons or holes by embedding the QD in a vertical (growth direction) diode structure and applying a vertical electric field that tunes the QD energy levels relative to the Fermi level set by the doping [7,12]. This same vertical electric field is often used to tune the QD emission wavelength via the Stark shift or, for QDMs, via indirect optical transitions [13–16]. Lateral electric fields have also been used to fine-tune the emission energies, fine-structure splittings [17–19], and spin lifetime [20], but these lateral fields have been applied in the absence of growth-direction (vertical) fields and have typically relied on either neutral excitons or spontaneous optical charging of the QDs. Simultaneously applying both vertical and lateral electric fields to create a two-dimensional (2D) electric field profile in the vicinity of a single QD could achieve simultaneous control over charging, emission wavelength, and fine-structure splitting. Moreover, such a 2D electric field profile could be used to controllably induce spin properties for qubit applications. Hole spin mixing in QDMs, for example, offers a unique opportunity to execute coherent spin rotations without transverse magnetic fields, which eliminates problems with spin precession that inhibit nondestructive readout [11,21,22]. Two-dimensional vector electric fields are an important tool for controllably inducing and modulating such hole spin mixing [23].

In this paper, we describe the design, simulation, fabrication, and characterization of a three-electrode device that applies 2D electric fields to a single InAs QD. We first present a device design that achieves the desired electric field profiles while also achieving the device specifications needed for optical interactions. We then systematically analyze several device parameters, describe their potential impact on the generation of 2D electric field profiles, and show that a model that accounts for depletion and band bending is required. This analysis justifies the design choices made. We then describe the device-fabrication process and characterize a proof-of-concept device using microphotoluminescence. We demonstrate that this proof-of-concept device achieves the desired 2D-electric-field profiles by comparing microphotoluminescence bias maps of single-QD emission as a function of various applied-voltage configurations with the 2D field profiles

*doty@udel.edu

 © 2020 American Physical Society

computed by COMSOL MULTIPHYSICS simulations. We conclude with a discussion of potential device improvements and follow-up experiments.

II. DEVICE DESIGN AND SIMULATION

The major challenge in designing a device that can apply 2D electric fields to single QDs is accommodating the random nucleation sites that are typical of MBE-grown InAs QDs. To do so, the device should (i) contain multiple optical apertures that can be used to locate and characterize single QDs, (ii) apply semiuniform electric fields around the QD location; (ii) generate electric fields with control over both the direction and the magnitude so that the effects of applied voltages can be fully understood from optical measurements; and (iv) be easily fabricated with a high yield. These are the criteria that guide our device-design discussion.

The design of the three-electrode device with one optimal set of parameters is shown in Fig. 1(a). The individual active part of our device consists of three electrodes patterned around a GaAs mesa with an intrinsic doping level less than 1×10^{15} cm^{-3}. The mesa has a trapezoidal shape with a 550-nm-wide bottom, and the sidewalls have a slope of 15°. The InAs QDs are embedded 50 nm above the bottom of the GaAs mesa. Two lateral electrodes are patterned on the side of the mesa, with a sidewall coverage slightly above the height of the QDs. The top electrode has a 250×250 nm^2 wide aperture, allowing optical access to the QD from the top of the wafer. The aperture size is chosen to be around one wavelength of light for efficient optical coupling. There is a 15-nm semitransparent Ti layer under the optical aperture to guarantee a uniform electric potential on the mesa top surface. This individual unit can be fabricated repeatedly across the entire QD wafer to increase the chances of finding one functional QD.

In devices with only a vertical *p*-*i*-*n* junction or only a pair of lateral electrodes, the electric field can be inferred accurately through a one-dimensional band diagram. In contrast, the 2D electric field profile of a multielectrode structure can have a very complicated dependence on the bias voltages applied to each electrode. We calculate the electric field of the three-electrode device using COMSOL MULTIPHYSICS simulations with the semiconductor model. The details of the simulation model are similar to those presented by Mohiyaddin *et al.* [24]. For nonpolar semiconductors such as GaAs, we use 0.8 V as the Schottky barrier height for the Ti/Au metal contact [25,26]. We know that the Fermi level will approach the defect level at low temperature, which is calculated through the intrinsic doping concentration. We keep the voltage between +1 and −1 V so that the field is relatively small and consistent across all of our discussions. Figures 1(b)–1(d) show the electric field profile generated under a vertical bias [Fig. 1(b)], a lateral bias [Fig. 1(c)], and an asymmetric bias [Fig. 1(d)]. In each case the voltage computationally applied to each electrode is indicated. As these figures show, the device is capable of generating a semiuniform vertical [Fig. 1(b)] and lateral [Fig. 1(c)] electric field near the QD region. Moreover, it can generate a 45° electric field with a set of carefully selected voltages, as shown in Fig. 1(d). These types of electric field can be used to apply an on-demand 2D electric field to a single QD.

Next, we briefly discuss the influence of the background doping level, mesa size, and lateral-electrode sidewall coverage on the device performance. We analyze the effects of these parameters on both fabrication feasibility and the ability to apply large and tunable vector electric fields. This analysis supports the design choices reported in Fig. 1.

A. Background doping

GaAs grown by MBE typically has some level of background *p*-type doping that inevitably affects the width of the depletion layer in the device. Figure 2 shows the

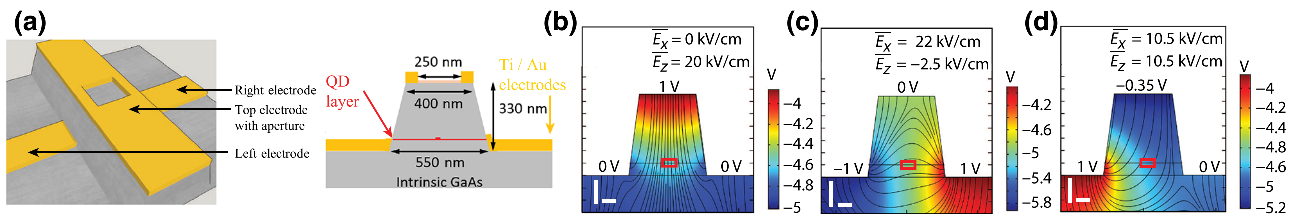

FIG. 1. (a) Optimal device geometry and (b)–(d) its electric field profile with various applied-voltage configurations. The vertical and horizontal scale bars (white) at the lower left of each panel are both 100 nm. The colored contour map shows the field potentials in volts. The electric field lines are included to indicate the direction of the electric field. The electric field values are referenced to the vacuum, which is taken to be at 0 V. The combination of the applied voltages (e.g., −1, 0, and 1 V), the band gap, and the work function results in calculated electric field values of approximately −4 to −6 V, which sets the range for the color-bar scales we use. This representation is used in all subsequent figures depicting the spatial variation of field potentials. The text inset in each panel indicates the average lateral (x) and vertical (z) electric field over the region in the center of each mesa at the height of the QD layer (red boxes). (b) A vertical bias that generates a uniform growth-direction electric field. (c) A lateral bias that generates a semiuniform in-plane electric field. (d) A 45°-field profile generated with custom voltages on three electrodes.

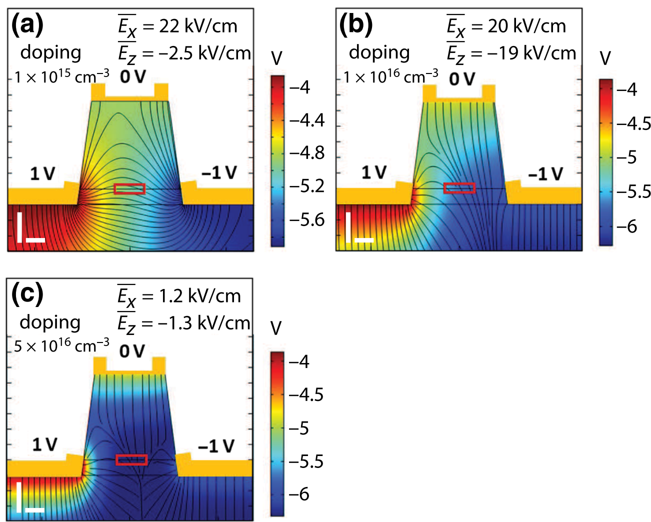

FIG. 2. Electric field profiles of the QD region (red box) under a constant lateral bias for various intrinsic doping levels. (a) A uniform lateral electric field is obtained with $1 \times 10^{15}\,\mathrm{cm}^{-3}$ intrinsic doping. (b) A diagonal electric field is obtained under the same lateral bias when the intrinsic doping is increased to $1 \times 10^{16}\,\mathrm{cm}^{-3}$. (c) A very weak electric field forms at the center of the mesa when the intrinsic doping is increased to $5 \times 10^{16}\,\mathrm{cm}^{-3}$. The field lines in the middle of the device with high doping do not bunch or cross. Rather, the very small and relatively uniform electric potential in the middle of the device leads to electric field lines that are so closely spaced that they cannot be distinguished on the scale of this figure.

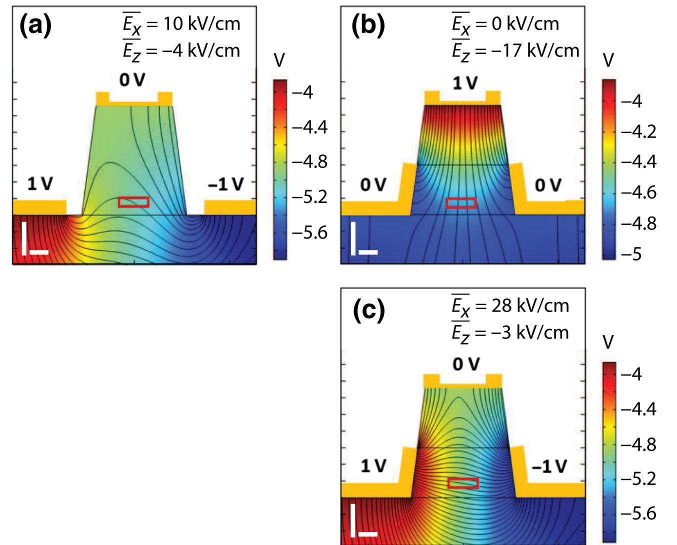

FIG. 3. Electric field profiles of the QD region (red box) under various biases and lateral-electrode geometries. (a) A diagonal electric field profile results when lateral electrodes are deposited 50 nm from the bottom edge of the mesa. (b),(c) Uniform electric field profiles under a vertical bias (b) and a lateral bias (c) can be achieved with lateral electrodes covering half of the mesa sidewall.

effect of intrinsic doping on the magnitude and direction of the electric field. As the background doping level increases from $1 \times 10^{15}\,\mathrm{cm}^{-3}$ [Fig. 2(a)] to $1 \times 10^{16}\,\mathrm{cm}^{-3}$ [Fig. 2(b)], the electric field profile under a lateral bias changes from a semiuniform lateral electric field to a diagonal electric field. When we further increase the background doping to $5 \times 10^{16}\,\mathrm{cm}^{-3}$ [Fig. 2(c)], the electric field magnitude drops by more than a factor of 10. Compared with all the other parameters, the background doping has the most-significant impact on the ability of the device to apply large and directional 2D electric fields.

B. Lateral electrode coverage

Figure 3 shows the electric field profile for different lateral-electrode configurations. All other device parameters are kept the same as for the optimal device model shown in Fig. 1. When the lateral electrodes end 50 nm from the bottom of the mesa, as shown in Fig. 3(a), the electric field uniformity and magnitude decrease. Consequently, an antisymmetric bias between the lateral electrodes (e.g., +1 and −1 V as depicted) does not generate a uniform lateral electric field near the QD region. This somewhat surprising result occurs because of different band bending at the two metal-semiconductor interfaces subjected to opposite voltages (+1 and −1 V). Figures 3(b) and 3(c) consider the opposite condition—sidewall coverage that is much larger than that depicted and simulated in Fig. 1. Specifically, Figs. 3(b) and 3(c) show the electric field profile under a vertical [Fig. 3(b)] and a lateral [Fig. 3(c)] bias when we increase the lateral-electrode sidewall coverage to 150 nm. The electric fields generated by these biases are uniform and the direction control is straightforward. However, fabricating such a geometry with high yield across the entire wafer can be extremely challenging. The optimal sidewall coverage depicted and simulated in Fig. 1 offers an acceptable balance between performance and fabrication yield.

C. Mesa width

Figure 4 shows the effect of the mesa width on the magnitude and uniformity of the lateral electric field. Three examples with different width at the bottom of the mesa are shown; all other parameters are the same as the optimal parameters described above. When the mesa is as wide as 800 nm [Fig. 4(a)], we see a nearly 40% drop in the total magnitude of the electric field compared with the optimal case [Fig. 4(b)], and a significant increase in the vertical component of the electric field. When the mesa width is reduced to 300 nm [Fig. 4(c)], we see a significant reduction in the vertical fringe field and a 100% increase in the lateral electric field component, both of which are desirable. However, besides the significant challenges of fabricating such narrow mesas, such a device geometry also requires the size of the optical aperture at the top of

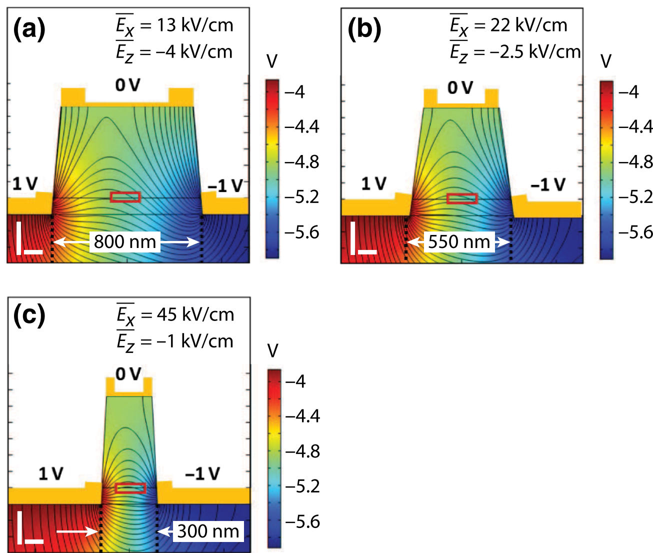

FIG. 4. Electric field profiles of the QD region (red box) under a constant lateral bias with various mesa sizes. (a) An 800-nm mesa yields a diagonal field profile under a lateral bias. (b) A 550-nm mesa yields a semiuniform lateral electric field profile with a 10% vertical component. (c) A 300-nm mesa yields a uniform lateral field profile, but reduced vertical outcoupling of light in the 1-μm region.

the device to be decreased below one wavelength (typically on the order of 1 μm for InAs QDs), which can significantly decrease the optical-coupling efficiency. The 550-nm mesa width used in our device design offers a compromise between the best electric field configuration and the fabrication and optical-performance requirements.

III. DEVICE FABRICATION

We grow our QDs using MBE on an intrinsic GaAs(001) substrate. We first grow 500-nm unintentionally doped GaAs on top of the substrate. We then deposit approximately 1.7 monolayers of InAs for QD nucleation and truncate the height of the dots with a 2.7-nm GaAs partial cap and subsequent flush of the exposed In at elevated temperature. We then grow 280-nm unintentionally doped GaAs on top of the QD. We stop the substrate rotation briefly during QD growth to form a QD density gradient, allowing us to locate a region of the wafer with relatively low QD density such that, on average, only one to three QDs lie within each device. We perform Hall-effect measurements to determine that the unintentionally doped GaAs is slightly p type with a bulk carrier concentration of $5 \times 10^{16}\,\mathrm{cm}^{-3}$. This background doping is far from the optimal level of $1 \times 10^{15}\,\mathrm{cm}^{-3}$ to generate large 2D electric fields, as discussed in Sec. II, but still allows us to accomplish the objective of building a proof-of-concept device that demonstrates the desired two-dimensional-electric-field behavior.

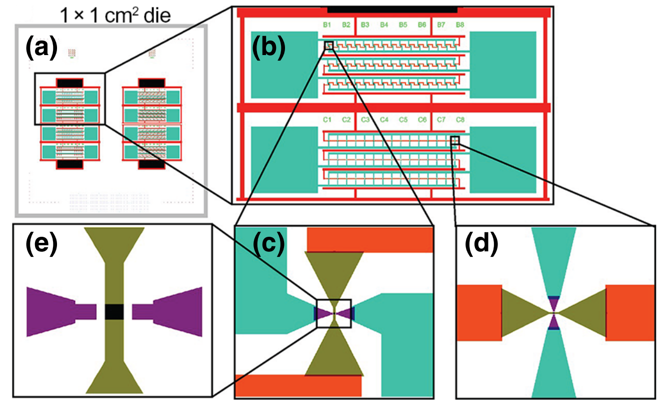

FIG. 5. Device layout viewed at different magnifications. (a) Two chips can be fabricated on a 1 × 1 cm^2 die. (b)–(d) Layout for one chip with (c) [100]-direction lateral electrodes and (d) [010]-direction lateral electrodes. (e) Active area of the device. The aperture size is later adjusted during the fabrication.

The device layout is presented in Fig. 5. As shown in Fig. 5(a), each 1 × 1 cm^2 die has two 3 × 5 mm^2 blocks. Each block consists of four segments. Each segment contains 45 individual three-electrode-device units as shown in Figs. 5(c)–5(e). Two segments in each block are designed to apply lateral electric fields along the [100] direction; the other two blocks apply lateral electric fields along the [010] direction. Figure 5(b) provides an expanded view of the top-two segments of the left block. The two orthogonal lateral-electrode configurations are shown in Figs. 5(c) and 5(d). In all cases the top electrode used to apply vertical electric fields (red) sits on top of the mesa (see Fig. 1) and is continuous as it threads through the entire segment and connects to the large bonding pads (black). The lateral electrodes (green and purple) are patterned around the mesa and connected to the large green bonding pads so that the 45 devices in each segment are connected in parallel. The purple areas distinguish the portions of the lateral electrode deposited in a separate fabrication step so as to obtain the desired precision in the electrode location and sidewall coverage, as illustrated in Fig. 5(e). An optical aperture [black square in Fig. 5(e)] can be fabricated on the top electrode for out-of-plane optical access. The size of the patterns used for lithography are varied on the basis of the fabrication conditions (e.g., desired undercut) so that the device dimensions after fabrication match the design and simulation results.

We use electron-beam lithography to fabricate the device because the fabrication requires a layer-to-layer alignment error smaller than 10 nm. Figure 6 shows the key fabrication steps for this device. We first fabricate the top electrode (20-nm Ti plus 100-nm Au) using a lift-off process with a PMMA/MMA [poly(methyl methacrylate)/methyl methyacrylate] bilayer resist and electron-beam metal deposition. We then pattern the

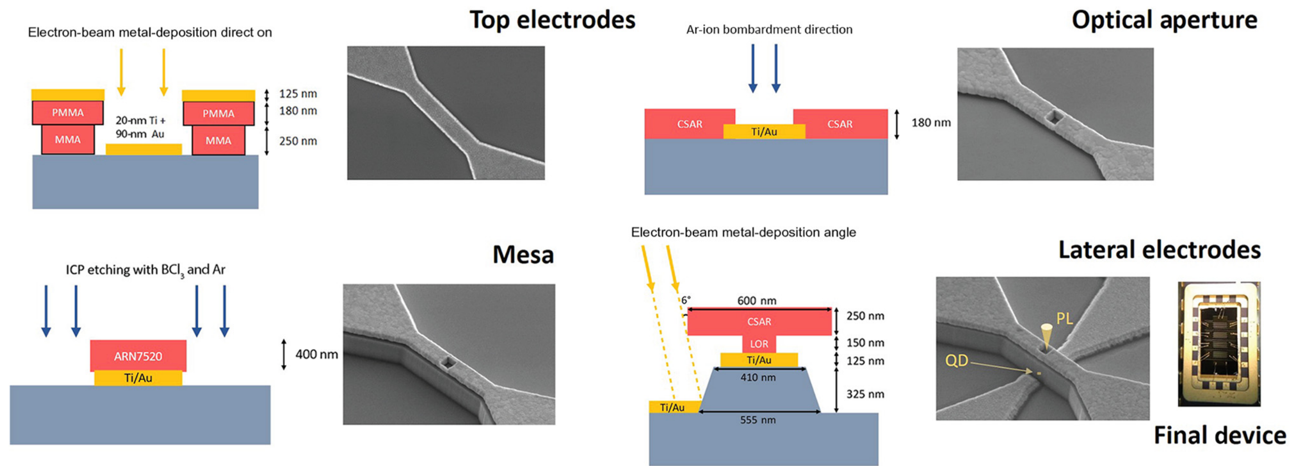

FIG. 6. Key fabrication steps. Top left: Top-electrode metal deposition with bilayer resist. Top right: Optical-aperture etching with ion milling. Bottom left: Mesa etching with ICP. Bottom right: Lateral electrode deposition with angle calculated from SEM pictures. CSAR, our electron beam lithography resist; LOR, lift-off resist; MMA, methyl methacrylate.

aperture on the top electrode and use ion milling to etch away the Au. The ion-milling-etching recipe has high selectivity between Au and Ti so that the etch can stop at the Ti layer without damaging the underlying GaAs. The 20-nm Ti is semitransparent in the near-infrared (NIR) wavelength range, which allows optical characterization from the top. We then etch the mesa by BCl_3 inductively-coupled-plasma (ICP) etching, creating the trapezoidal mesa shape with the angled sidewalls. The angle of the sidewall is engineered by our balancing the chemical etching and the physical bombardment during the ICP etching. To fabricate the lateral electrodes, we use a bilayer resist, angled electron-beam metal deposition, and a final lift-off process. To guarantee that the lateral electrodes cover the mesa sidewalls, we first characterize the resist geometry using SEM, and then calculate the appropriate metal-deposition angle. The result is a 50-nm-high sidewall coverage that brings the metal up the mesa sidewall to just above the QD layer. To maximize our chances of observing a single QD in an aperture, we fabricate 180 individual apertures on a 5×3 mm^2 die, each one identical to the structure shown in Fig. 5(e). These electrodes are connected to 500×500 μm^2 bonding pads for wire bonding.

IV. DEVICE CHARACTERIZATION

A. Microphotoluminescence

We mount the sample in an ARS-DMX20 cryostat to study its photoluminescence (PL) at 8 K. We use a light-emitting-diode light to locate each aperture and a 5-μW 780-nm cw laser to excite the quantum dots. We focus the laser light with a NIR objective with a spot size close to the diffraction limit so that we will only excite QDs from a single aperture. We collect the PL through two OD5 900-nm long-pass filters and measure the energy of the emitted photons with a NIR spectrometer equipped with a liquid-nitrogen-cooled CCD. We use a Keithley 2230 multichannel voltage source to apply voltages to the device.

We first survey all the apertures to find the ones that contain a single QD, and then apply voltages for detailed studies of the selected apertures. Figure 7 shows the PL-intensity graphs from four different apertures (QDs) under different electric field conditions. In every case we verify that the device current (leakage current) remains below 500 μA throughout the range of voltages applied during the PL measurement. This upper bound on the leakage current confirms that there are no shorts between the three electrodes. We choose the value of 500 μA as an upper bound because it is close to our current detection limit. For all data presented in the left column, we ground the two lateral electrodes and apply the voltage V to the top electrode. We name this bias configuration “the vertical bias.” Under these conditions, we observe asymmetric charging in the PL map for all four QDs presented here. We assign the charge states on the basis of excitation-power dependence and literature reports of the typical energy shifts between various charge configurations [12,13,27]. For example, in QD a, the positively charged state (X^+) with energy 1317.8 meV becomes visible at -0.3 V, as indicated by the dashed line. The neutral exciton state (X) with energy of 1314.3 meV and the neutral biexciton state (XX) with energy of 1313.1 meV disappear at the same voltage. Although the neutral exciton states disappear when we apply a sufficiently large positive voltage to the top electrode, we do not see a negatively charged state appear. We therefore attribute the loss of signal from the neutral exciton states to electric fields that allow at least one carrier to escape the QD before recombination. We observe similar PL features in QD b, QD c, and QD d. The precise energy

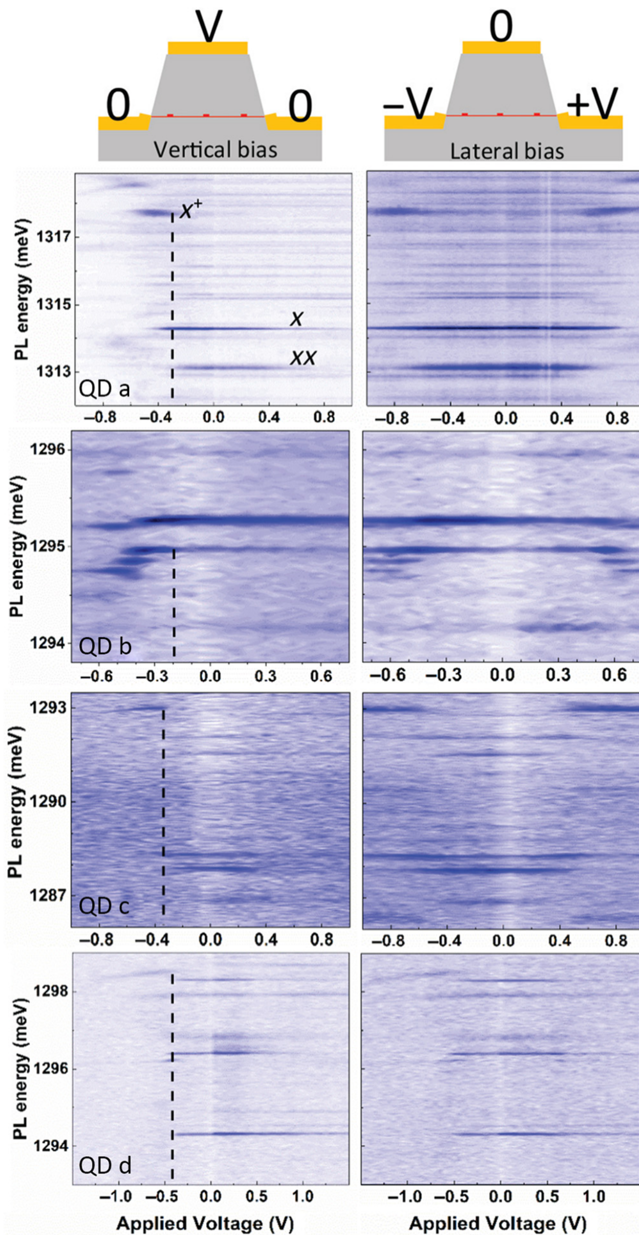

FIG. 7. Microphotoluminescence of four different QDs from four different apertures on the three-electrode device. The left panel shows the PL-intensity map under a vertical bias, and the right panel shows the PL-intensity map under a lateral bias. The x axis represents the applied voltage V in each case, and the y axis represents the PL energy observed from each aperture.

differences between the neutral exciton state and the positively charged state vary between different dots. This is common in MBE-grown InAs QDs and is likely due to the different electron-hole interaction strengths that result from variations in QD size and composition.

For the data presented in the right column, we apply equal and opposite voltages to the two lateral electrodes while grounding the top electrode. We name this bias configuration "the lateral bias." We apply the same magnitude of voltages as for the vertical bias. In this case, we observe charging in each QD exactly analogous to what is observed in the left column for the vertical-bias condition, but with different symmetry. For example, in QD a the positively charged exciton emerges symmetrically at both positive and negative lateral biases ($V = 0.6$ V and $V = -0.6$ V). The same symmetric charging PL map can be seen in QD b and QD c. This symmetric charging pattern is representative of the majority of the apertures that we survey and is different from the asymmetric charging pattern observed for all apertures under a vertical bias. Very occasionally, we observe an asymmetric charging pattern under a lateral bias, as shown in QD d. The faint charged line around 1298.5 meV shows up only on one side of the lateral-bias PL map, in contrast to the symmetric charging pattern observed in QD a, QD b, and QD c. In the next section we explain how these charging patterns arise from and validate the existence of 2D vector electric fields.

B. COMSOL MULTIPHYSICS simulation

The charging pattern under the vertical or lateral bias can be explained through the electric field profile presented in Fig. 8. We consider first the vertical-bias condition. Figures 8(a) and 8(b) show the electric potential of the three-electrode device when we apply a vertical bias. As shown in Fig. 8(a), when we apply -1 V to the top electrode, the bias forms a large potential gradient near the two lateral electrodes, while the rest of the mesa's potential remains relatively flat. As shown in Fig. 8(b), when we apply $+1$ V to the top electrode, the bias forms a large potential gradient near the top of the mesa. The experimental data show that charging happens only when we apply a negative voltage to the top electrode, indicating that holes are electrically injected into the QDs by the lateral electric fields formed on both sides of the mesa. Wavelength-dependent PL (see Fig. 9 in the Appendix) also confirms the possibility of a hole reservoir forming near the wetting layer. We do not observe hole charging when we apply a positive voltage to the top electrode because the lateral electric field is small. For QDs near the center of the mesa, holes can be injected through the large potential gradient near the positive lateral electrodes when the top voltage is negative, thus resulting in the observed asymmetric charging patterns in the left hand column in Fig. 7.

We now consider what happens under lateral-bias conditions. The colored surface maps in Figs. 8(c) and 8(d) show the electric potential when we apply lateral biases. We can see that large potential gradients can be formed near the electrode with the positive bias, and the electric field remains flat near the electrode with negative voltage. For QDs near the center of the mesa, holes can be

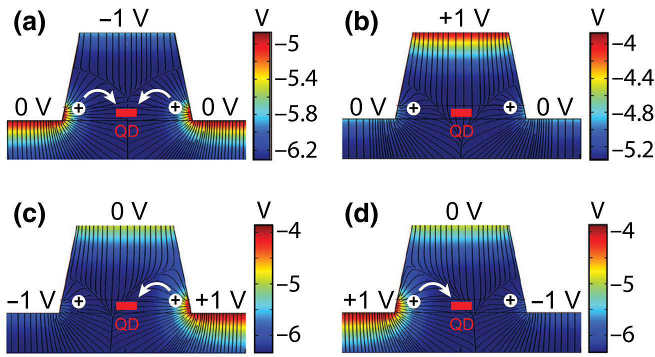

FIG. 8. Charging predictions from COMSOL MULTIPHYSICS simulations. The simulations show the electric field direction (lines) and electric field potential (color) under (a),(b) vertical-bias and (c),(d) lateral-bias conditions. Arrows indicate the possible charging processes in each case.

injected through the large potential gradient near the positive lateral electrode, regardless of which side it is on. Consequently, we observe symmetric charging patterns in the right-hand maps in Figs. 7(a)–7(c). We believe that the asymmetric charging pattern observed in Fig. 7(d) results when the QD is located relatively close to one electrode, resulting in charging only when that nearby electrode is positive. Taken together, the microphotoluminescence data presented in Fig. 7, specifically the different charging patterns observed for vertical-bias and lateral-bias conditions, demonstrate that our device creates both vertical and lateral electric fields.

V. DISCUSSION

Throughout our device design, we follow the principle that the device should be easy to operate, meaning that a vertical bias should generate only vertical electric fields, and vice versa. It is entirely possible that the optimal device does not have to follow this principle and could be operated with preprogrammed voltage configurations that are neither intuitive nor simple. Such a design approach will, however, require significantly more simulation time to systematically explore all possible voltage combinations and their corresponding electric field profiles. We also note that the COMSOL MULTIPHYSICS simulations, which are consistent with the experimental data, indicate that this device has generated a 2D electric field. Another clear indication of the 2D electric field control would be the observation of a Stark shift from both the vertical and lateral electric fields. Although we observe a Stark shift of around 200 μeV at high voltages, as indicated in Fig. 7(d), the overall magnitude is very small. This indicates that the magnitude of the electric field at the QD is small. This is a direct consequence of the high p-type-defect density in the intrinsic GaAs of the material used for these particular devices. This high doping level increases the depletion

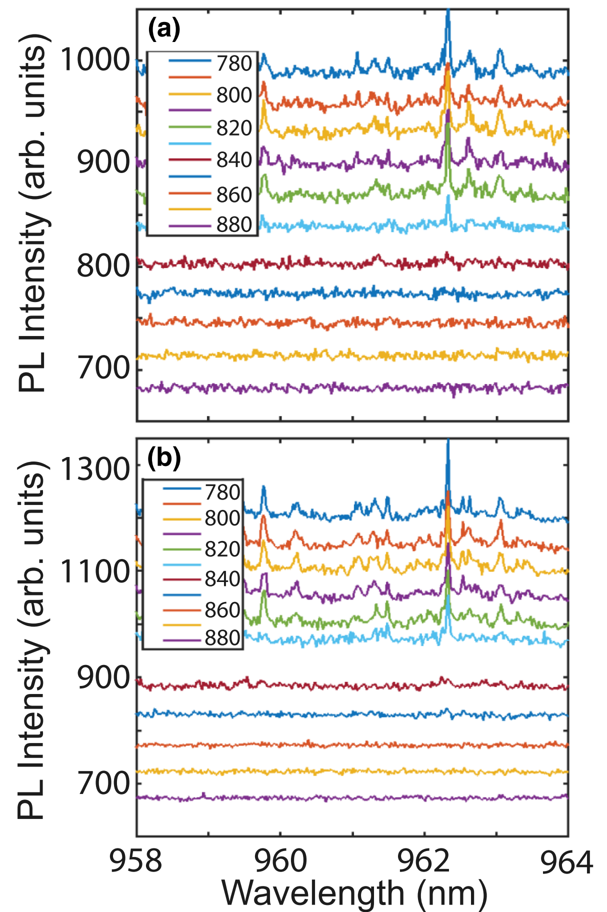

FIG. 9. Excitation-wavelength dependence of PL from a single QD. The same wavelength threshold for QD PL is found in measurements with excitation powers of (a) 5 μW and (b) 50 μW. The insets indicate the excitation wavelength used for each trace. Each trace is offset along the y axis for clarity.

width and reduces the band bending near the Schottky contact. Future device iterations can seek to lower this background doping level and/or introduce a δ-doping layer near the QDs to charge a single QD with an electron or a hole.

VI. CONCLUSION

We report the design and fabrication of a three-electrode device that can apply 2D electric fields to single QDs embedded in an unintentionally doped GaAs matrix. We characterize single QD PL under different bias configurations and observe asymmetric charging patterns under vertical biases and symmetric charging patterns under lateral biases. Combining the experimental data with electric field simulations, we deduce that these charging events likely originate from electrically injected holes whose tunneling into the QDs is induced by lateral electric fields. This device thus demonstrates an important step toward the generation of devices that apply arbitrary 2D electric

fields to single QDs or QDMs and, separately, demonstrates deterministic charging of single QDs arising from lateral electric field components.

ACKNOWLEDGMENT

We acknowledge financial support from the NSF (DMR-1505574). We also acknowledge support from Allan Bracker and Michael Yakes of the Naval Research Laboratory, who helped us to grow test samples and provided valuable suggestions. Finally, we acknowledge support from Iulian Codreanu, Kevin Lister, Paul Horng, and Scott McCracken of the UD Nanofabrication Facility, who helped us to develop the fabrication recipes used.

APPENDIX: WAVELENGTH-DEPENDENT PL

To further understand the charging behavior reported in Fig. 7, we conduct wavelength-dependent PL measurements of these QDs. The PL of QD c as a function of excitation wavelength is shown in Fig. 9. The PL intensity begins to drop significantly when the excitation wavelength increases from 820 to 830 nm and reaches zero for excitation wavelengths longer than 830 nm. This excitation-wavelength threshold does not change with different excitation powers, as compared in Figs. 9(a) and 9(b).

The fact that the PL suddenly quenches when the excitation wavelength increases from 820 to 830 nm indicates a lack of carriers available for excitation when the laser wavelength is longer than 830 nm. This wavelength corresponds to the energy of the p-type defects formed during growth. These defects push the Fermi level close to the valence-band edge, and large band bending can be formed near the Schottky contact. At 8 K, holes in these defects are likely to freeze or relax to the wetting-layer valence band because their energy levels are close. We suspect that holes trapped in the wetting layer are the reservoir for the electrically injected holes observed in the PL spectra.

[1] X. Ding, Y. He, Z.-C. Duan, N. Gregersen, M.-C. Chen, S. Unsleber, S. Maier, C. Schneider, M. Kamp, S. Höfling, *et al.*, On-Demand Single Photons with High Extraction Efficiency and Near-Unity Indistinguishability from a Resonantly Driven Quantum dot in a Micropillar, Phys. Rev. Lett. **116**, 020401 (2016).

[2] N. Somaschi, V. Giesz, L. De Santis, J. C. Loredo, M. P. Almeida, G. Hornecker, S. L. Portalupi, T. Grange, C. Antón, J. Demory, *et al.*, Near-optimal single-photon sources in the solid state, Nat. Photonics **10**, 340 (2016).

[3] L. Hanschke, K. A. Fischer, S. Appel, D. Lukin, J. Wierzbowski, S. Sun, R. Trivedi, J. Vučković, J. J. Finley, and K. Müller, Quantum dot single-photon sources with ultra-low multi-photon probability, npj Quantum Inf. **4**, 43 (2018).

[4] M. Davanco, J. Liu, L. Sapienza, C.-Z. Zhang, J. V. M. Cardoso, V. Verma, R. Mirin, S. W. Nam, L. Liu, and K. Srinivasan, Heterogeneous integration for on-chip quantum photonic circuits with single quantum dot devices, Nat. Commun. **8**, 889 (2017).

[5] C. Dory, K. A. Fischer, K. Müller, K. G. Lagoudakis, T. Sarmiento, A. Rundquist, J. L. Zhang, Y. Kelaita, and J. Vučković, Complete coherent control of a quantum dot strongly coupled to a nanocavity, Sci. Rep. **6**, 25172 (2016).

[6] K. Hennessy, A. Badolato, M. Winger, D. Gerace, M. Atatüre, S. Gulde, S. Fält, E. L. Hu, and A. Imamoğlu, Quantum nature of a strongly coupled single quantum dot–cavity system, Nature **445**, 896 (2007).

[7] R. J. Warburton, Single spins in self-assembled quantum dots, Nat. Mater. **12**, 483 (2013).

[8] M. F. Doty, J. I. Climente, A. Greilich, M. Yakes, A. S. Bracker, and D. Gammon, Opportunities for single hole-spin control using delocalized states of quantum dot molecules, J. Phys.: Conf. Ser. **245**, 012002 (2010). IOP Publishing.

[9] D. Gammon, E. S. Snow, B. V. Shanabrook, D. S. Katzer, and D. Park, Fine Structure Splitting in the Optical Spectra of Single Gaas Quantum Dots, Phys. Rev. Lett. **76**, 3005 (1996).

[10] K. Yamaguchi, K. Yujobo, and T. Kaizu, Stranski-krastanov growth of inas quantum dots with narrow size distribution, Jpn. J. Appl. Phys. **39**, L1245 (2000).

[11] M. F. Doty, J. I. Climente, A. Greilich, M. Yakes, A. S. Bracker, and D. Gammon, Hole-spin mixing in inas quantum dot molecules, Phys. Rev. B. **81**, 035308 (2010).

[12] X. Zhou, S. Sanwlani, W. Liu, J. H. Lee, Z. M. Wang, G. Salamo, and M. F. Doty, Spectroscopic signatures of many-body interactions and delocalized states in self-assembled lateral quantum dot molecules, Phys. Rev. B. **84**, 205411 (2011).

[13] E. A. Stinaff, M. Scheibner, A. S. Bracker, I. V. Ponomarev, V. L. Korenev, M. E. Ware, M. F. Doty, T. L. Reinecke, and D. Gammon, Optical signatures of coupled quantum dots, Science **311**, 636 (2006).

[14] A. S. Bracker, M. Scheibner, M. F. Doty, E. A. Stinaff, I. V. Ponomarev, J. C. Kim, L. J. Whitman, T. L. Reinecke, and D. Gammon, Engineering electron and hole tunneling with asymmetric inas quantum dot molecules, Appl. Phys. Lett. **89**, 233110 (2006).

[15] M. F. Doty, M. Scheibner, I. V. Ponomarev, E. A. Stinaff, A. S. Bracker, V. L. Korenev, T. L. Reinecke, and D. Gammon, Electrically Tunable g Factors in Quantum dot Molecular Spin States, Phys. Rev. Lett. **97**, 197202 (2006).

[16] W. Liu, S. Sanwlani, R. Hazbun, J. Kolodzey, A. S. Bracker, D. Gammon, and M. F. Doty, In situ tunable g factor for a single electron confined inside an inas quantum dot molecule, Phys. Rev. B. **84**, 121304 (2011).

[17] B. D. Gerardot, S. Seidl, P. A. Dalgarno, R. J. Warburton, D. Granados, J. M. Garcia, K. Kowalik, O. Krebs, K. Karrai, A. Badolato, *et al.*, Manipulating exciton fine structure in quantum dots with a lateral electric field, Appl. Phys. Lett. **90**, 041101 (2007).

[18] M. E. Reimer, M. Korkusiński, D. Dalacu, J. Lefebvre, J. Lapointe, P. J. Poole, G. C. Aers, W. R. McKinnon, P. Hawrylak, and R. L. Williams, Prepositioned single quantum dot in a lateral electric field, Phys. Rev. B. **78**, 195301 (2008).

[19] K. Kowalik, O. Krebs, A. Lemaitre, S. Laurent, P. Senellart, P. Voisin, and J. A. Gaj, Influence of an in-plane electric field on exciton fine structure in inas-gaas self-assembled quantum dots, Appl. Phys. Lett. **86**, 041907 (2005).

[20] G. Moody, C. McDonald, A. Feldman, T. Harvey, R. P. Mirin, and K. L. Silverman, Electronic Enhancement of the Exciton Coherence Time in Charged Quantum Dots, Phys. Rev. Lett. **116**, 037402 (2016).

[21] X. Zhou and M. Doty, Design of 4-electrode optical device for application of vector electric fields to self-assembled quantum dot complexes, J. Appl. Phys. **116**, 163101 (2014).

[22] S. E. Economou, J. I. Climente, A. Badolato, A. S. Bracker, D. Gammon, and M. F. Doty, Scalable qubit architecture based on holes in quantum dot molecules, Phys. Rev. B. **86**, 085319 (2012).

[23] X. Ma, G. W. Bryant, and M. F. Doty, Hole spins in an inas/gaas quantum dot molecule subject to lateral electric fields, Phys. Rev. B. **93**, 245402 (2016).

[24] F. A. Mohiyaddin, F. G. Curtis, M. N. Ericson, and T. S. Humble, Simulation of silicon nanodevices at cryogenic temperatures for quantum computing, Nanotechnology **27**, 42 (2016).

[25] W. Mönch, Barrier heights of real schottky contacts explained by metal-induced gap states and lateral inhomogeneities, J. Vacuum Sci Technol B: Microelectron. Nanometer Struct. Process., Meas., Phenom. **17**, 1867 (1999).

[26] H. Altuntaş, Ş. Altındal, S. Özçelik, and H. Shtrikman, Electrical characteristics of au/n-gaas schottky barrier diodes with and without sio2 insulator layer at room temperature, Vacuum **83**, 1060 (2009).

[27] M. E. Ware, E. A. Stinaff, D. Gammon, M. F. Doty, A. S. Bracker, D. Gershoni, V. L. Korenev, Ş. Bădescu, Y. Lyanda-Geller, and T. L. Reinecke, Polarized Fine Structure in the Photoluminescence Excitation Spectrum of a Negatively Charged Quantum dot, Phys. Rev. Lett. **95**, 177403 (2005).